Supplementary Information for "Driven Topological Transitions in Active Nematic Films"

David P. Rivas,[1] Tyler N. Shendruk,[2] Robert R. Henry,[1] Daniel H. Reich,[1] and Robert L. Leheny*[1]

[1] *Department of Physics and Astronomy, Johns Hopkins University, Baltimore, MD, USA, 21218*
[2] *Interdisciplinary Centre for Mathematical Modelling and Department of Mathematical Sciences, Loughborough University, Loughborough, UK, LE11 3TU*

I. LIST OF SUPPLEMENTARY VIDEOS

Video S1: Microscopy video of the merger of two +1/2 defects into a +1 topological vortex in an active nematic film due to stresses produced by a rotating disk. The images in Fig. 2 are taken from this video.
Video S2: Lattice-Boltzmann simulation of the merger of two +1/2 defects into a +1 topological object. The images in Fig. 3 are from this simulation.
Video S3: Microscopy video of the decay of a topological vortex into two +1/2 defects. The images in Figs. 4a-d are taken from this video.
Video S4: Lattice-Boltzmann simulation of the decay of a +1 topological object into two +1/2 defects. The images in Figs. 4e-h are from this simulation.
Video S5: Microscopy video of active nematic films in the presence of a rotating disk during a period in which no topological vortex forms. Note that the +1/2 defects in proximity to the disk tend strongly to circulate anti-clockwise around the disk.
Video S6: Lattice-Boltzmann simulation of a contractile active nematic system influenced by the imposed stress field produced by a counter-clockwise rotating disk. Parameters are unchanged from Videos S2 and S4, except with the activity ζ negative rather than positive.

II. SAMPLE PREPARATION

A. Active Gel Fabrication

The active gel was fabricated by combining appropriate quantities of microtubules, ATP, and a premix solution that contained kinesin clusters, anti-bleaching agents, polyethylene glycol as a depletant, an ATP regeneration system, and buffer, as described in Ref. [1]. The microtubules and premix were provided by Marc Radilla from the Biological Materials Facility at Brandeis University. The final concentration of polyethylene glycol was 0.8% (w/v) and the final concentration of ATP was typically 1.4 mM. The microtubules were labeled with AlexaFluor 647 to enable video tracking of moving bundles using fluorescence microscopy. Prior to formation of an active nematic film, a dilute quantity of ferromagnetic nickel disks was added to the mixture. The disks (radius 20 μm, thickness 300 nm) were fabricated using photolithography methods described elsewhere [2]. The disks had a permanent magnetic moment μ that was parallel to the disk face and had a magnitude of approximately 1.6×10^{-8} emu (at an applied field of 30 G), as determined from magnetically induced rotations of the disks at a bare oil-water interface.

B. Sample Cell Fabrication

Sample cells were fabricated from two glass slides approximately 1" × 0.5" that were first cleaned in hot water containing 1% Hellmanex (Hellma) solution and sonicated for ∼10 minutes. One slide was made hydrophilic by coating with polyacrylamide, and the other slide was hydrophobically treated using Aquapel (Pittsburgh Glass Works). The hydrophilic treatment involved first sonicating the cleaned glass in ethanol for ten minutes, then rinsing with deionized (DI) water and sonicating in 0.1 M KOH, also for approximately ten minutes. A solution of DI water and 2% w/v acrylamide was placed under vacuum for at least 15 minutes prior to adding 0.035% tetramethylethylenediamine and 0.7 g/L ammonium persulfate. The slides were soaked in a solution of 98.5% ethanol, 1% acetic acid, and 0.5% 3-(trimethoxysilyl) propylmethacrylate for roughly 15 minutes, rinsed again, and then soaked overnight in the acrylamide solution. The slides were rinsed in DI water and dried prior to use. The hydrophobic treatment involved coating the glass in Aquapel for approximately one minute then rinsing with DI water and drying. Thin strips of double-sided tape were placed on the surface of the hydrophobic slides to create two channels of approximate dimensions 2 cm × 0.2 cm in which two active nematic films were created. The hydrophilic slides were then laid on top and pressed down onto the tape.

Fluorinated oil (HFE 7500, RAN Biotechnologies) was pipetted into a channel via capillary action. The active gel containing a dilute dispersion of magnetic disks was immediately pipetted into the same channel displacing the oil except for a thin layer adjacent to the hydrophobic surface. The sides of the cell were then sealed with Norland Optical Adhesive 81 (Norland Products), and the cell was centrifuged for 10-15 minutes at 800 rpm (103 g) driving the microtubules to the oil-water interface and leading to formation at the interface of a dense film of microtubule bundles with nematic order. The centrifugation also caused the disks to go to the oil-water interface; however, they did not embed in the film but remained in the aqueous phase at a height $d = 3$ to 8 μm

above the film and oriented with their faces parallel to the film, as depicted schematically in Fig. 1(a).

III. VIDEO MICROSCOPY DETAILS

Observations of the disks and film were made with an inverted microscope (Nikon TE2000) and a 20X objective (Nikon, CFI LWD DL 20X). Disks selected for measurements were sufficiently isolated from other disks that the influence of other disks could be safely ignored. (As shown in Fig. 6, the effect of the rotating disks on the active nematic films extends at most about 300 micrometers from the disk center. For all the results presented in the paper, the distance between the disks employed in measurements and any neighboring disks was many times greater than this length scale.) Videos were captured using a Flare CameraLink (IOIndustries) camera with a frame rate of 1 to 5 frames per second. An exposure time of one over the frame rate was typically used for fluorescent imaging. Image analysis was conducted using custom Python scripts, particle imaging velocimetry (PIV) in Matlab, and ImageJ.

Magnetic fields were applied using an array of solenoids with soft magnetic cores that was mounted on the microscope stage. Two sets of four solenoids positioned symmetrically above and below the sample position allowed for application of fields in arbitrary direction. The feedback-regulated current to the coils was computer controlled using custom Labview software, as described elsewhere [3]. In the experiments, magnetic fields $\mathbf{B}$ rotating in the plane of the film at angular frequency ν were applied. The fields caused the disks to rotate, also at angular frequency ν, with the disk faces parallel to the active nematic film. Specifically, as the field and disk rotated, the magnetic moment μ of the disk lagged $\mathbf{B}$ by an angle θ such that the magnetic torque on the disk $\mu B \sin\theta$ was balanced by the drag torque on the disk from the surrounding fluid. Due the active turbulence in the nearby active nematic film, this drag torque could fluctuate so that θ fluctuated noticeably if the magnitude of the rotating field was too small. The magnitudes of the fields employed in the experiments were typically 80 to 120 G, which was large enough to ensure that the disks rotated at the prescribed rate, which varied over 20 Hz $\leq \nu \leq$ 120 Hz, without noticeable fluctuations.

We note that disks rotating with their faces at an angle to the film are unstable due to the asymmetry in the drag they experience, and as a result, such disks quickly flip sideways so that they rotate up on end much like a coin spinning on its edge. Occasionally, disks were observed to flip up on end in this way. Fluid-dynamics calculations in COMSOL of disks rotating in this geometry and found that the stress they impose on the film includes both azimuthal and radial components. However, the radial component is periodic, reversing direction with a frequency of twice the disk rotation frequency. In the experiments, we found the rotating disks that flipped up on end affected the active nematic films in a manner that was qualitatively like the rotating disks whose faces were parallel to the film, including driving the formation of topological vortices. However, all results presented in the paper were obtained from measurements in which the disk face remained parallel to the film.

Measurements of the heights of the disks relative to the films involved adjusting a motorized z-stage on the microscope between positions at which the film and the disk were in focus. An objective with lower depth of field (Nikon, CFI Plan Fluor ELWD 40X) was employed in these measurements for more precise determination of the height, and we estimate the precision of the height measurements to be ± 2 μm. Once a rotating disk reached a steady-state height, its height showed no measurable variation with time; therefore, we consider the disk height to be essentially fixed.

IV. ESTIMATE OF STRESS ON ACTIVE NEMATIC FILM FROM ROTATING DISK

Estimates of the hydrodynamic stress imposed on the film by a disk rotating in the water layer above the film were performed using COMSOL's Computational Fluid Dynamics module. As an example, Fig. S1 displays the stress at the film surface as a function of horizontal distance r from the disk center computed for a 40 μm-diameter disk positioned 35 μm above the film and rotating at 80 Hz. The surface of the rotating disk imposed a no-slip boundary condition creating a shear flow in the water, and due to the large difference in viscosities between the water and film, we approximated the film as a stationary surface that also imposed a no-slip boundary condition on the water's flow. As shown in the inset, the stress decays as r^{-4} at large r, while at small values of r corresponding to the film directly under the disk, the stress increases linearly with r.

V. SIMULATION DETAILS

A. Active Nematohydrodynamics

The ATP-powered microtubule-bundles/kinesin-complexes mixture at an oil/water interface is simulated as a 2D active nematic film. Simulations numerically solve the incompressible active nematohydrodynamics equations of motions [4, 5] for the local velocity $\mathbf{u}(\mathbf{r};t)$ and nematic order $\mathbf{Q}(\mathbf{r};t)$ fields, which obey the coupled Navier-Stokes and Beris-Edwards equations

$$\partial_t \rho + \nabla \cdot (\rho \mathbf{u}) = 0 \tag{S1}$$

$$\rho D_t \mathbf{u} = \nabla \cdot \mathbf{\Pi} - \gamma \mathbf{u} + \mathbf{g} \tag{S2}$$

$$D_t \mathbf{Q} - \mathcal{S} = \Gamma \mathbf{H}. \tag{S3}$$

Sufficiently small Mach number ensures near incompressibility, making $\partial_i u_i = 0$ and ρ constant.

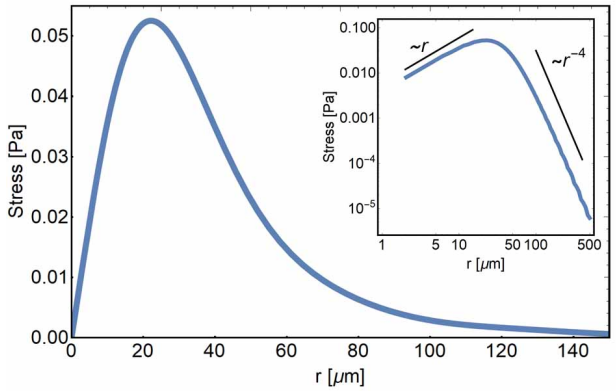

Fig. S1. Computed stress on a film surface due to shear flow in the adjacent water created by a 40-μm-diameter disk rotating at 80 Hz at a height of 35 μm above the film, plotted as a function of distance r from the center of the disk. The inset shows the stress on a log-log scale.

The second equation (Eq. S2) is the Navier-Stokes equation, in which $D_t = \partial_t + u_k\partial_k$ is the material derivative and Π_{ij} are the components of the stress. The term g_i represents the external force density due to the rotating disk (see Section V B). The Brinkman term γu_i introduces a friction coefficient γ into the film flows [6], which arises from a lubrication approximation for the dissipation within the thin viscous oil layer between the active film and the bottom boundary [7]. The friction coefficient screens hydrodynamic flows over distances much larger than $\sim \sqrt{\eta/\gamma\rho}$, where η is the viscosity of the film. We define the strain rate $E_{ij} = (\partial_i u_j + \partial_j u_i)/2$, vorticity $\mathcal{W}_{ij} = (\partial_i u_j - \partial_j u_i)/2$, and $\mathcal{Q}_{ij} = Q_{ij} + \delta_{ij}/3$. The stresses within the film have four contributions [8]:

1. The Newtonian viscous stress $\Pi^{\rm visc}_{ij} = 2\eta E_{ij}$.

2. The hydrostatic pressure $\Pi^{\rm press}_{ij} = -P\delta_{ij}$, which is taken to be constant.

3. The nematic contribution, which itself has symmetric and antisymmetric contributions.

   (a) The symmetric terms are $\Pi^{\rm LC,symm}_{ij} = 2\lambda\mathcal{Q}_{ij}Q_{kl}H_{lk} - \lambda H_{ik}\mathcal{Q}_{kj} - \lambda\mathcal{Q}_{ik}H_{kj} - \partial_i Q_{kl}\frac{\delta F}{\delta(\partial_j Q_{lk})}$, where H_{ij} is the molecular field and F is the free energy. The alignment parameter λ acts to mix upper and lower convective derivative terms.

   (b) The antisymmetric contribution is $\Pi^{\rm LC,anti}_{ij} = Q_{ik}H_{kj} - H_{ik}Q_{kj}$.

4. The active stress is directly proportional to the liquid crystaline order $\Pi^{\rm act}_{ij} = -\zeta Q_{ij}$. The activity ζ is positive for extensile active nematics, such as the microtubule/kinesin-based films, and negative for contractile active nematics.

The final equation (Eq. S3) models the evolution of the nematic order tensor. The left-hand side of Eq. S3 describes the generalized material derivative accounting for the co-rotational advection, $\mathcal{S}_{ij} = (\lambda E_{ik} + \mathcal{W}_{ik})\mathcal{Q}_{kj} + \mathcal{Q}_{ik}(\lambda E_{kj} - \mathcal{W}_{kj}) - 2\lambda\mathcal{Q}_{ij}Q_{kl}\partial_k u_l$. The ΓH_{ij} term describes the relaxation of the order parameter towards the free energy minimum, where Γ is a collective rotational diffusivity. The molecular field

$$\mathbf{H} = -\frac{\delta F}{\delta \mathbf{Q}} + \frac{\mathbf{I}}{3}\mathrm{Tr}\left[\frac{\delta F}{\delta \mathbf{Q}}\right] \tag{S4}$$

is symmetric and traceless and is related to the functional derivative of the free energy F. The free energy is the sum of two contributions $F = \int d^3r \left[f^{\rm LdG} + f^{\rm el}\right]$, a Landau-de Gennes bulk free energy density $f^{\rm LdG} = AQ_{ij}Q_{ji}/2 + BQ_{ij}Q_{jk}Q_{ki}/3 + C\left(Q_{ij}Q_{ji}\right)^2/4$ and an elastic deformation free energy $f^{\rm el} = K\partial_k Q_{ij}\partial_k Q_{ij}$ assuming a single elastic Frank coefficient K.

B. Hybrid Lattice Boltzmann Simulation Details

The equations of motion (Eq. S1-S3) are solved using a hybrid lattice Boltzmann/finite difference scheme [4]. The Navier-Stokes equation (Eq. S2) is solved using the lattice Boltzmann algorithm on a D3Q15 grid. On the other hand, Eq. S3 is solved using a finite difference predictor-corrector algorithm.

Simulations are performed on a two-dimensional domain of size 400×400 with periodic boundary conditions for 1.5×10^5 time steps. The discrete space and time steps define the simulations units (su; see Section V C), which are used in this section. The density is $\rho = 1$ and the hydrostatic pressure is $P = 1/4$. The Landau–de Gennes coefficients used are $A = 0$, $B = -0.3$, and $C = 0.3$, while the rotational diffusivity is $\Gamma = 0.34$, consistent with our previous works [9]. The dynamic viscosity is $\eta = 2/3$. The friction coefficient is $\gamma = 3 \times 10^{-4}$. The Frank elasticity is $K = 0.1$, while the activity is $\zeta = 5 \times 10^{-3}$ unless otherwise stated. Three values of the alignment parameter are considered, $\lambda = \{0.3, 0.7, 0.9\}$. Simulation parameters were chosen to ensure that the disk size in simulation units was large compared to the discrete lattice spacing.

To account for the stresses on the nematic film due to the ferromagnetic nickel colloidal disk, we model the rotation resulting from constant external magnetic torque. For simplicity, the disk is fixed in place above the film. The density of the disk is chosen to be 100 times that of the film. In addition to the magnetic torque, the dissipative drag is $-\zeta_{\rm aq}\Omega$, where Ω is the resulting rotation rate of the disk and $\zeta_{\rm aq} = 10$ is the rotational drag coefficient of the disk in the aqueous solution. The chosen values ensure that the disk's dynamics are over damped. The rotation of the disk is hydrodynamically coupled to the active flows within the film. We model the effect to be local with coupling only occurring directly below the

effective hydrodynamic radius of the disk. The hydrodynamic radius $R^{\mathrm{H}} = 25.2$ is taken to be three times the geometric radius of the disk, which accurately captures the experimentally measured position of the maximum average velocity of the film. The hydrodynamic drag imposed by the rotating disk on the film, which in the experiments is mediated by the viscous coupling through the intervening aqueous layer, is modeled as a force density proportional to the differences in velocity, $\mathbf{g} = \zeta_{\text{d-f}} [\mathbf{v}(\mathbf{r}, t) - \mathbf{u}(\mathbf{r}, t)]$, where the velocity of each element of the disk is $\mathbf{v}(\mathbf{r}, t) = \Omega(t)\, \hat{z} \times \mathbf{r}$. The equal and opposite force density on the disk produces a torque on the disk that slightly modifies the rotation rate.

C. Simulation Units

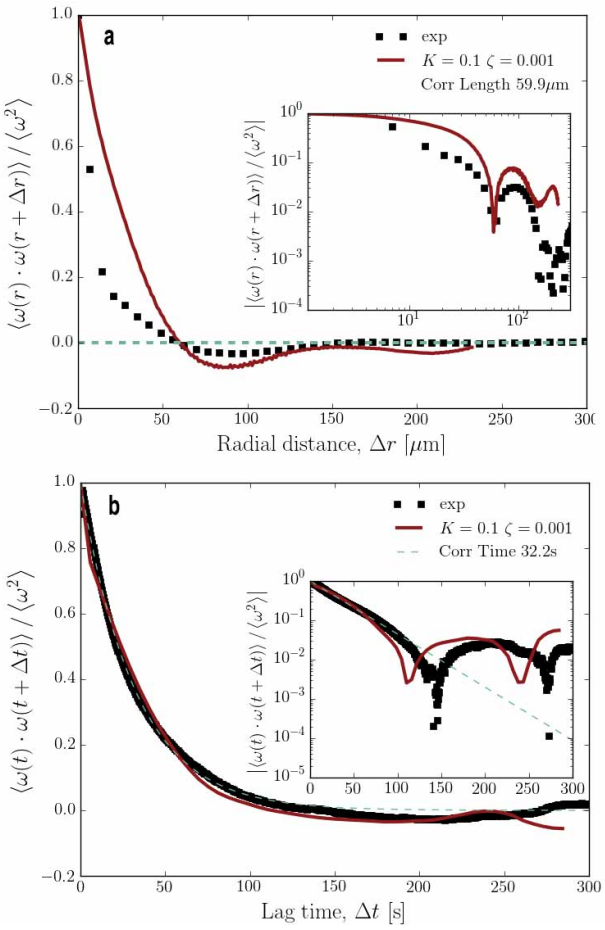

Fig. S2. The vorticity auto-correlation functions for experiments (black squares) and hybrid-LB simulations (red lines). Panel (A) shows the same-time spatial auto-correlation function and panel (B) shows the temporal auto-correlation function. The simulation parameters used are $\gamma = 3 \times 10^{-4}$ and $\lambda = 0.3$.

In this study, care has been taken to match simulation units (su) to the physical conditions of the experimental system. Numerical simulations are unitless and appropriate parameters must be chosen to identify possible scalings to convert numerical results to physical units. We converted simulation length and time scales to the experiments by comparing decorrelations within the experimental and simulated vorticity fields. To determine the length unit conversion we matched the zero crossing point of the spatial vorticity auto-correlation function (Fig. S2(a)). Experimentally, the correlation length measured in this way is 60 μm. Positive correlation appears more pronounced in the idealized simulations in the near field, as do anti-correlations in the intermediate range. In our case, fitting the zero crossing point reproduces the extent of the anti-correlation range. This produces the conversion of 1 su : 2.38 μm.

The unit time conversion is determined by fitting an exponential decay to the short-lag region of the temporal vorticity auto-correlation function (Fig. S2(b)). The experimental correlation time is found to be approximately 30 s. This is seen to produce good agreement, both in the short-lag positive correlation and in the intermediate-time anti-correlation. This produces the conversion of 43.7 su : 1 s. We use these length and time units for the simulations presented in the main text. These conversions are for a specific experimental activity and oil layer thickness — we expect them to vary slightly for different experimental realizations.

VI. CHARACTERIZATION OF NEMATIC ORDER

A. +1/2-Defect Orientation Pair Correlation Function

Figure S3 displays the orientation correlation function between +1/2 defects in an active nematic film as a function of the separation Δr of the defects. The correlation function is defined as the average value of the dot product of the orientation unit vectors, $\langle \hat{\psi}(0) \cdot \hat{\psi}(\Delta r) \rangle$. Nearby +1/2 defects tend to be anti-aligned, as seen by the negative values of the correlation function at small separations.

B. Nematic Correlation Length

Figure S4 displays a time and spatial average of the nematic director correlation function, defined as $\langle (\hat{n}(0) \cdot \hat{n}(\Delta r))^2 \rangle$, obtained from analyzing a video of an active nematic film spanning 12 minutes and covering a field of view of 570 μm $\times$ 570 μm. Due to short-range nematic ordering in the active nematics, the correlation function is positive at small separations. For random relative orientations of the director, the average value of the correlation function is 0.5, which is the value reached at large separations. At intermediate separations of approximately 120 μm, the correlation function drops below

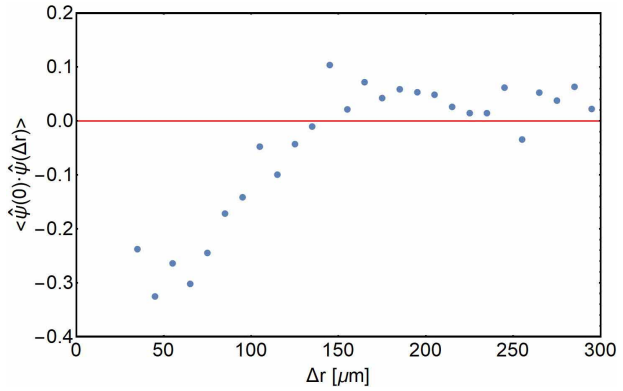

Fig. S3. The orientation correlation function of +1/2 defects as a function of defect separation Δr. The negative values at short separations indicate that nearby +1/2 defects tend to be anti-aligned.

0.5. We identify the nematic correlation length, shown by the vertical dashed line in the Fig. 6, as the location of the minimum of this region. This distance also roughly equals the average separation between defects ($\sim$130 μm).

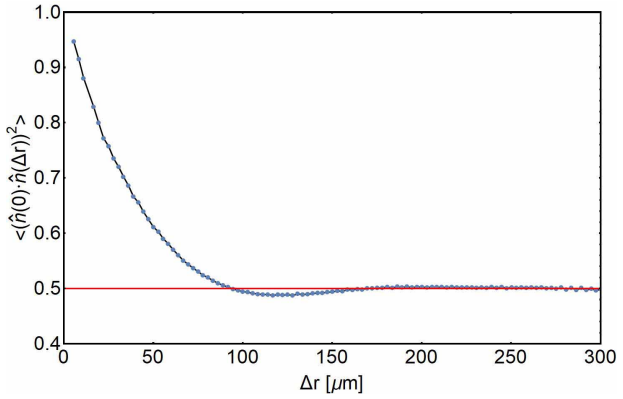

Fig. S4. The nematic correlation function, defined as the average of the squared dot product of the director at positions separated by Δr. The results shown are obtained from averaging over a movie of 12 minutes in duration.

VII. IMAGE ANALYSIS DETAILS

A. Determination of Speed and Vorticity of the Flow in the Active Nematic Films

To quantify the velocity and vorticity in the active nematic films as shown in Fig. 5, we employed particle image velocimetry (PIV) techniques [10] to measure the displacement of microtubule bundles in subsections of the film between adjacent video frames. These results were binned and averaged by distance relative to the center of the disk, as determined by the mean location of the disk in the image pair to produce the results shown in Fig. 6(a) and (e).

B. Quantifying Vortex Decay Dynamics

The decay of a topological vortex proceeded by the circularly symmetric director field around the defect core elongating into an elliptical shape in which two +1/2 defects oriented toward each other (*i. e.*, with each defect orientation vector ψ pointing toward the other defect) could quickly be identified. To characterize the time evolution of the decay process, we tracked this elongation and then the trajectories of the +1/2 defects by hand using the image processing program ImageJ. An example pair of trajectories is shown in Fig. S5. The inset shows the distance between the +1/2 defects as a function of time. The specific decay time in which the +1 vortex is replaced by two well-defined +1/2 defects is not clearly defined, but was about 5 s after the start of the elongation into an elliptical director field. In Fig. S6 we plot five additional examples of the separation distance of +1/2 defect pairs produced in topological vortex decays versus time. The speeds of the +1/2 defects as they propagated away from one another were not measurably different from the typical speeds of the +1/2 defects in the film moving solely as a consequence of the activity.

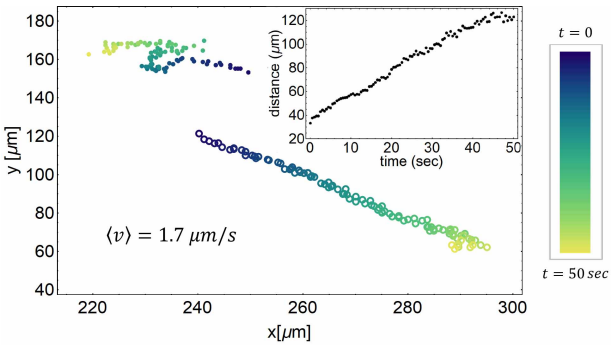

Fig. S5. Example trajectories of the vertices of the collapsing elliptical +1 topological structure and the subsequent +1/2 defects. The inset shows their separation versus time. The average speed at which the two features separated was about 1.7 μm/s. For comparison, the average speed of the +1/2 defects in the film was 1.7 $\pm$ 0.5μm/s.

C. Characterization of the Velocity Profile around a Topological Vortex

Individual microtubule bundles in the vicinity of vortices were tracked using the custom Python code Trackpy [11], which after thresholding found the centroids of the brightest connected features in each image.

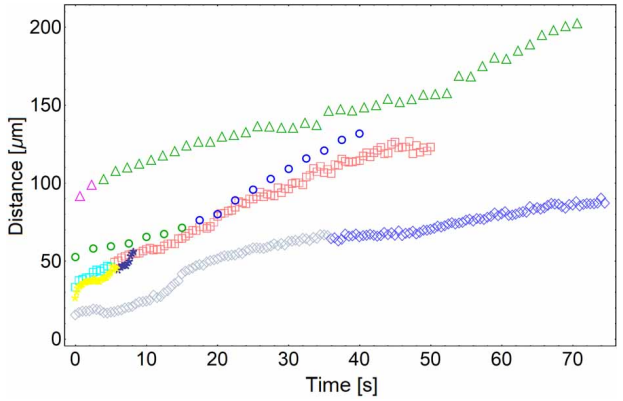

Fig. S6. Distance between ends of the collapsing vortices as a function of time for several cases of vortex decay. The change of color of the data points indicates the approximate time at which the elongating +1 topological object became two distinct +1/2 defects.

These features were then linked using Trackpy's link algorithm. The trajectories were hand filtered to select only the region of active nematic with director oriented azimuthally about the vortex. The distance of each feature from the vortex core was determined, and the measured speeds of features were averaged over bins of size 10 μm, resulting in the red data points in Fig. 7. The blue data points in the same figure were produced using a similar method, however, since no topological vortex was present, no filtering of the trajectories was performed. The uncertainties were found by calculating the standard error of the mean of the ensemble average in each bin. Averages of the speeds of each feature were taken rather than an overall average in order to limit the effect of correlations in the data which could skew the mean and underestimate the uncertainty.

VIII. COMSOL CALCULATIONS OF VELOCITY PROFILE AROUND A VORTEX

As discssed in Sec. 3.3 of the manuscript, a region of the film in vicinity of the rotating disk experienced a large increase in flow velocity upon formation of a +1 topological vortex (see Fig. 7). To model this flow profile, we performed hydrodynamic calculations numerically using COMSOL's Computational Fluid Dynamics module. The calculations mimicked the experimental geometry of a disk rotating in a fluid with the viscosity of water (10^{-3} Pa·s) at a set height (35 μm) above a film of thickness 300 nm and viscosity η_f, which was varied in the calculations to optimize the agreement with the experimental velocity profile. The space below the film was similarly treated as a fluid with viscosity matching that of the oil in the experiments (10^{-3} Pa·s). Several thicknesses for the oil layer were tested in the calculations, and the resulting velocity profile in the film was insensitive to the layer thickness as long as it was greater than ≈ 1 μm. Since the region of enhanced film velocity in the experiments typically coincided with the region of active nematic centered on the disk in which the director field was oriented in the azimuthal direction, we modeled the film as a circle of radius R matching the size of this region. As a boundary condition we set the velocity at the edge of the circle equal to the experimentally measured speed of the surrounding active nematic (approximately 1 μm/s). Over the lifetime of a vortex, the region of azimuthally oriented director field typically fluctuated. For example, for the vortex analyzed to produce the velocity profile in Fig. 7, R varied between approximately $R = 60$ μm and $R = 90$ μm during the measurements. Therefore, we calculated velocity profiles in films with R ranging from 60 to 90 μm and took the average of these curves to compare with the data. This process was repeated for different values of η_f to find the optimal agreement with the experimental data. For instance, Fig. S7 shows a set of curves that were averaged to produce the calculated curve shown in Fig. 7.

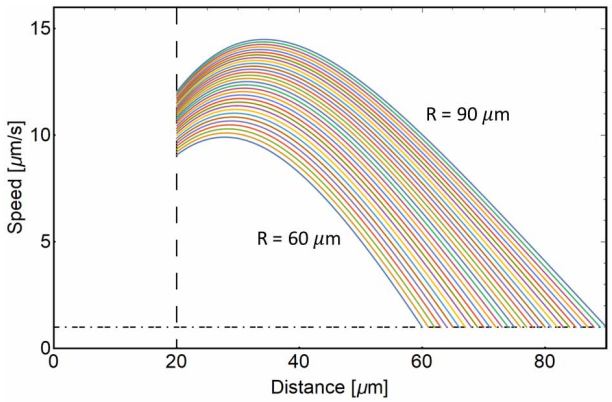

Fig. S7. Calculated fluid velocity in a circular region of film as a function of distance from the center of the disk for a range of circle radii from 60 to 90μm in steps of 1μm. There is a boundary condition of v = 1μm/s at the outer boundary (shown by the horizontal dot-dashed line). The vertical dashed line represents the radius of the disk. These example velocity profiles were calculated using the same parameters that produced the calculated curve shown in Fig. 7 of the main text.

[1] S. J. DeCamp, G. S. Redner, A. Baskaran, M. F. Hagan, and Z. Dogic, Orientational order of motile defects in active nematics, Nature Materials **14**, 1110 (2015).

[2] J. B. Rovner, D. S. Borgnia, D. H. Reich, and R. L. Leheny, Elastic and hydrodynamic torques on a colloidal disk within a nematic liquid crystal, PRE **86**, 041702 (2012).

[3] M. H. Lee, C. P. Lapointe, D. H. Reich, K. J. Stebe, and R. L. Leheny, Interfacial hydrodynamic drag on nanowires embedded in thin oil films and protein layers, Langmuir **25**, 7976 (2009).

[4] D. Marenduzzo, E. Orlandini, M. E. Cates, and J. M. Yeomans, Steady-state hydrodynamic instabilities of active liquid crystals: Hybrid lattice boltzmann simulations, Phys. Rev. E **76**, 031921 (2007).

[5] S. P. Thampi, R. Golestanian, and J. M. Yeomans, Vorticity, defects and correlations in active turbulence, Philosophical Transactions of the Royal Society A: Mathematical, Physical and Engineering Sciences **372**, 20130366 (2014).

[6] S. P. Thampi, R. Golestanian, and J. M. Yeomans, Active nematic materials with substrate friction, Phys. Rev. E **90**, 062307 (2014).

[7] H. Bruus, Theoretical Microfluidics, Oxford Master Series in Physics (Oxford University Press Oxford, 2008).

[8] C. Denniston, D. Marenduzzo, E. Orlandini, and J. Yeomans, Lattice boltzmann algorithm for three-dimensional liquid-crystal hydrodynamics, Philosophical Transactions of the Royal Society of London. Series A: Mathematical, Physical and Engineering Sciences **362**, 1745 (2004).

[9] T. N. Shendruk, K. Thijssen, J. M. Yeomans, and A. Doostmohammadi, Twist-induced crossover from two-dimensional to three-dimensional turbulence in active nematics, Phys. Rev. E **98**, 010601 (2018).

[10] W. Thielicke and E. J. Stamhuis, Pivlab - time-resolved digital particle image velocimetry tool for matlab (version: 2.00) (2014).

[11] D. B. Allan, T. A. Caswell, N. Keim, F. Boulogne, R. W. Perry, and L. Uieda, trackpy: Trackpy v0.3.3, (2014).